

A Lévy flight for electrons in graphene: superdiffusive-to-diffusive transport transition

Diego B. Fonseca,¹ Luiz Felipe C. Pereira,^{2,*} and Anderson L. R. Barbosa^{1,†}

¹*Departamento de Física, Universidade Federal Rural de Pernambuco, Recife - PE, 52171-900, Brazil*

²*Departamento de Física, Centro de Ciências Exatas e da Natureza, Universidade Federal de Pernambuco, Recife - PE, 50670-901, Brazil*

In this work we propose an electronic Lévy glass, analogous to a recent optical realization. To that end, we investigate the transmission of electrons in graphene nanoribbons in the presence of circular electrostatic clusters, whose diameter follow a power-law distribution. We analyze the effect of the electrostatic clusters on the electronic transport regime of the nanoribbons, in terms of its diffusion behavior. Our numerical calculations show that the presence of circular electrostatic clusters induces a transition from Lévy (superdiffusive) to diffusive transport as the energy increases. Furthermore, we argue that in our electronic Lévy glass, superdiffusive transport is an exclusive feature of the low-energy quantum regime, while diffusive transport is a feature of the semiclassical regime. We thus attribute the observed transition to the chiral symmetry breaking, once the energy moves away from the Dirac point of graphene.

I. INTRODUCTION

Graphene is a unique platform to emulate wave optics by electronic phenomena, since its linear dispersion relation at low excitation energy coincides qualitatively with the photon's dispersion [1–4]. This linear dispersion is due to the honeycomb lattice of graphene, which can be seen as a triangular Bravais lattice with a two-atom basis [5–7]. In graphene, charge carriers behave as massless relativistic Dirac fermions, and the lattice preserves chiral symmetry. These unique electronic properties give rise to Klein tunneling [8 and 9], where massless fermions can tunnel through a potential barrier with null reflection probability.

In this context, Ref. [10] reported the electronic analogue of Mie scattering in a graphene superlattice imbedded in a cylindrical electrostatic potential [11 and 12]. Mie scattering is an optical phenomenon which takes place when light waves are elastically scattered by spherical or cylindrical objects. Furthermore, Ref. [13] studied the effects of a regular array of electrostatic quantum dot clusters (EQDC) in otherwise pristine graphene nanoribbons, which induces a local deformation of the on-site potentials. Both theoretical predictions were confirmed in Ref. [1], which presented an experimental demonstration of an electronic analogue of Mie scattering by using a graphene superlattice as a conductor imbedded into a regular EQDC array. They were followed by other relevant work on the effect of circular electrostatic potentials in graphene [14–19].

The experimental setup of Ref. [1], inventively, reminds one of a remarkable optical wave transport work: *A Lévy flight for light* [20]. Lévy flights are a particular class of non-Gaussian random walks in which a heavy-tailed (power-law) distribution describes the step length during the walk [21]. Those flights are present in different fields of science such as the migration pattern of animals [22 and 23], transport in turbulent flows [24], optical wave transport [20, 25–29] and electronic transport [9, 30–33]. Lévy flights lead to superdiffusive transport,

which is characterized by a mean-square displacement growing faster than linear with time, i.e., $\langle x^2 \rangle \propto t^{\gamma_D}$, where $\gamma_D > 1$. Meanwhile, for $\gamma_D = 1$ we recover the regular diffusive transport regime [21, 34, and 35].

Ref. [20] developed an optical material in which the transport of light is governed by Lévy statistics: a Lévy glass. The material was fabricated by suspending titanium dioxide microspheres in sodium silicate, where the diameter of the microspheres followed a heavy-tailed distribution. The suspended microspheres are a scattering material with fractal structures, where the larger particles give origin to Mie scattering. Furthermore, since the configuration of microspheres is fixed in the Lévy glass, subsequent steps are correlated, in contrast to a standard Lévy walk, where the steps are all uncorrelated [36]. The authors of Ref. [20] observed that when the light is transmitted through the Lévy glass, it shows superdiffusive transport instead of regular diffusive transport. Therefore, the average transmission coefficient as a function of the device length L follows [20, 36, and 37]

$$\langle T \rangle = \frac{1}{1 + (L/\ell)^\gamma}, \quad (1)$$

where ℓ is the mean free path. When $\gamma = 1$, we have the usual behavior giving rise to regular diffusive transport. Whereas, when $\gamma < 1$, we have a slow decay of the transmission characterizing a superdiffusive transport regime.

In order to emulate the optical Lévy flight [20] with electrons, we propose an electronic Lévy glass (ELG) and develop realistic numerical calculations of the electronic transport through graphene nanoribbons imbedded into the EQDC, whose radii follow a heavy-tailed distribution, as shown in Fig. 1. We find that our ELG show a Lévy-to-diffusive transport transition as a function of the Fermi energy, which is a particular feature of the graphene honeycomb lattice. Furthermore, our analysis indicates that the most probable cause of the observed transition is the breaking of chiral symmetry, once the energy moves away from the Dirac point of graphene. Finally, we believe that the Lévy-to-diffusive transition

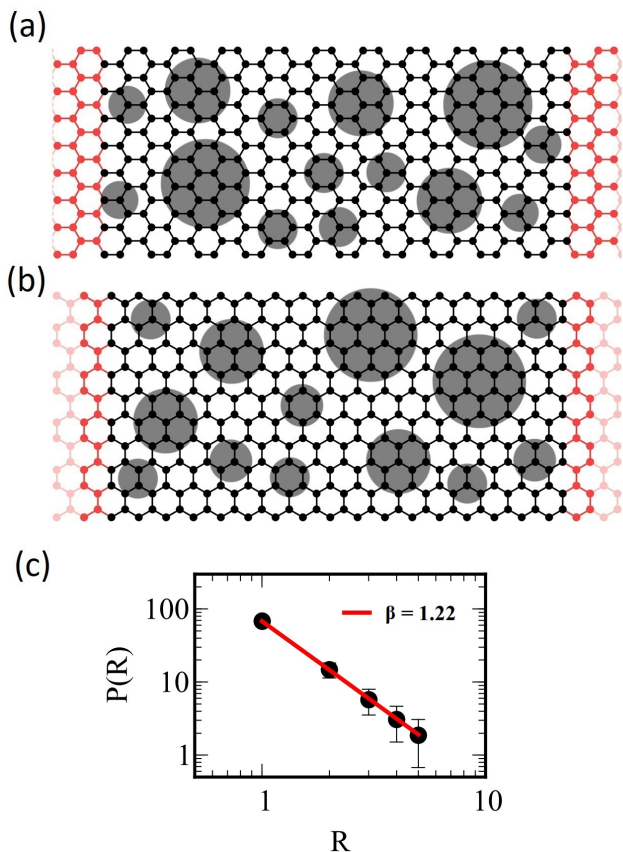


FIG. 1. Illustration of (a) AGNR and (b) ZGNR connected to two leads (red). Grey circles represent EQDC. (c) Histogram of cluster radii (symbols); the solid line is a fit obtained from Eq. (5) with $\beta = 1.22 \pm 0.01$.

can be experimentally verified by an adaptation of the experimental setup in Ref. [1].

II. MICROSCOPIC MODEL

We study the electronic transmission through graphene nanoribbons connected to two leads, and imbedded into randomly located EQDC, as illustrated in Fig. 1. The scattering matrix describing the electronic transport through the nanoribbons is given by [38]

$$S = \begin{bmatrix} r & t' \\ t & r' \end{bmatrix}, \quad (2)$$

where $t(t')$ and $r(r')$ are the transmission and reflection matrix blocks, respectively. The transmission coefficient can be calculated from the Landauer-Büttiker relation

$$T = \text{Tr}[tt^\dagger], \quad (3)$$

which is valid in the linear response regime. Numerical calculations of the transmission coefficient were performed with KWANT [39], which is a Green's function-based algorithm within the tight-binding approach.

The tight-binding Hamiltonian for graphene is given by

$$\hat{H} = -t_0 \sum_{\langle i,j \rangle} c_i^\dagger c_j + \sum_i \epsilon_i c_i^\dagger c_i, \quad (4)$$

where the indices i and j run over all lattice sites and $\langle i,j \rangle$ denotes first nearest neighbors. The first term in \hat{H} represents the usual electron hopping between lattice sites, c_i (c_i^\dagger) are the annihilation (creation) operators and t_0 is the hopping energy, which has a typical value of 2.7 eV [7]. The second term in the Hamiltonian is the electrostatic potential induced by the EQDC. Therefore, the on-site electrostatic potential ϵ_i will be $\epsilon_i = V$ when the site is inside the quantum dot area, and $\epsilon_i = 0$ otherwise.

The Hamiltonian in Eq. (4) is identical to the one in Ref. [13], which studied the effects of a regular array of EQDC in otherwise pristine graphene nanoribbons, and motivated the experiment developed in Ref. [1]. This is a deliberate choice which allows us to probe the effect of the Lévy-disorder on electronic transport, and to perform a direct comparison with a periodic disorder. Furthermore, Ref. [13] also did not consider edge passivation in the nanoribbons since it should not influence electronic transport significantly in the presence of EQDC. Finally, the EQDC are not expected to modify the hopping parameter significantly, and thus we consider the same hopping energy inside and outside the clusters, also in line with Ref. [13].

Figs. 1(a) and (b) illustrate armchair (AGNR) and zigzag (ZGNR) graphene nanoribbons, respectively, imbedded into the EQDC. In order to build the ELG, we follow four steps: 1) randomly select both a point on the lattice, which will be the center of the quantum dot, and the radius R of the quantum dot; 2) assign all sites inside the quantum dot area a constant electrostatic potential value $\epsilon_i = V$; 3) randomly select a new lattice point and radius: if the new quantum dot overlaps with a pre-existing one, begin step 3 again, otherwise go to step 2; 4) stop after 5000 consecutive failed attempts to introduce a new quantum dot. The maximum radius of the quantum dot is limited to one eighth of the lattice width without any loss of generality. In fact, this restriction is common in studies involving Lévy distributions because of the divergence of its second moment [21].

A Lévy distribution is characterized by the probability density of a random variable $P(R)$, which has a power-law tail [21, 33, and 40]. The probability density is given by

$$P(R) \propto \frac{1}{R^{\beta+1}}, \quad (5)$$

where $0 < \beta < 2$. If $0 < \beta < 1$, the first and second moments of $P(R)$ diverge because of heavy-tails, while for $1 \leq \beta < 2$ only the second moment diverges. Fig. 1(c) shows the radii histogram obtained from 10^4 different AGNR samples with width $W_A = 49.5a_0$ and length $L_A = 51.4a_0$, where $a_0 = 2.49 \text{ \AA}$ is the graphene lattice

constant. The histogram can be adjusted to the power law given in Eq. (5) with an exponent $\beta = 1.22 \pm 0.01$. Because of the Lévy distribution behavior, a set of quantum dots with radius R occupies approximately the same area as another set of quantum dots with a different radius. Similar behavior was reported by Ref. [20]. Furthermore, in our simulations the fraction of the nanoribbon area occupied by quantum dots is $42.24\% \pm 0.03$, and it remains unchanged for different device lengths L , widths and edge types.

III. RESULTS

To understand the effect of the EQDC on the average transmission coefficient, we build an ensemble of ELG for AGNR and ZGNR. We kept fixed the widths, $W_A = 49.5a_0$ and $W_Z = 49.6a_0$, and the electrostatic potential $V = 0.25t_0$, while varying the length up to $L_A = 1050.7a_0$ and $L_Z = 1050.5a_0$, respectively. Besides, for future comparison between honeycomb and square lattices, we also build a set of square lattices, which we refer to as two-dimensional electron gas (2DEG), with $W_{2D} = 50a_0$ and L_{2D} up to $1050a_0$.

We begin by plotting the transmission coefficient as a function of Fermi energy in Fig. 2(a) for $L_A = 1050.7a_0$ and $L_Z = 1050.5a_0$. For the ELG, the transmission (solid line) presents strong fluctuation due to EQDC, and is generally smaller when compared to the pristine nanoribbons (dotted lines). Meanwhile, Fig. 2(c) shows the average transmission through the AGNR as a function of length L for three different Fermi energies, $E/t_0 = 0.2, 0.34$ and 1.2 . The average transmissions (symbols) were calculated from a set of 6000 different ELG and conveniently normalised to range between 0 and 1. Fig. 2(d) is the equivalent for a ZGNR with $E/t_0 = 0.2, 0.4$ and 1.2 .

The average transmission of Figs. 2(c) and (d) decrease as power-law functions of length L . Therefore, we can fit the data with Eq. (1) and obtain the exponent γ for each Fermi energy. The exponent characterizes the diffusive ($\gamma = 1$) and superdiffusive ($\gamma < 1$) transport regimes. Figs. 2(c) and (d) show that for high Fermi energy ($E/t_0 = 1.2$) the exponent is $\gamma \simeq 1$ for both AGNR and ZGNR. Meanwhile, when we decrease the Fermi energy the exponent decreases to $\gamma \simeq 0.5$, which indicates a non-trivial Lévy-to-diffusive transport transition as the Fermi energy increases.

Before proceeding with our investigation, we could ask ourselves: *Is the average transmission behavior shown in Figs. 2(c) and (d) really due to the EQDC?* To answer this question, we first developed a numerical calculation of the transmission through nanoribbons with a constant electrostatic potential $\epsilon_i = V$ in all sites, at three different Fermi energies. Fig. 2(b) shows that for the AGNR the transmission remains almost constant as function of length (circles). As a second verification, we ran a numerical calculation with a typical Anderson disorder [41

and 42]. In this case, the electrostatic potential ϵ_i varies randomly from site to site according to a uniform distribution in the interval $(-V/2, V/2)$. Again, we found that for the AGNR the transmission remains almost constant as a function of length, Fig. 2(b) (squares). The same behavior was observed for a ZGNR, which leads to the conclusion that the Lévy-to-diffusive transition is indeed a consequence of the EQDC, and not due to some arbitrary electrostatic potential.

In order to characterize the Lévy-to-diffusive transition, it is convenient to relate the Fermi energy to the number of channels in the nanoribbon N . This dimensionless integer corresponds to the number of propagating wave modes in the ribbon, which is proportional to both the width W and the Fermi vector k_F through $N = k_F W / \pi$. Since our aim is to study electronic localization, we keep W fixed and increase the graphene length L tuning N only by the Fermi energy. If the width W is kept fixed, the electronic structure of each nanoribbon remains unchanged during the numerical calculation. Nonetheless, we have verified that the transition does not depend on W , as discussed below.

Fig. 3(a) shows the transmission coefficient of pristine AGNR, ZGNR and 2DEG as a function of the Fermi energy. The value at the plateaus corresponds to the number of channels, i.e. $T(E) = N$. For the AGNR (blue line), we have a relation between $E/t_0 = 0.02, 0.05, 0.08, \dots$ and $N = 1, 2, 3, \dots$, similarly for ZGNR (red line) and 2DEG (black line). Knowing the relation between the Fermi energy and the number of channels, we can study how the exponent γ varies as a function of N .

Fig. 3(b) shows the exponent γ as a function of N ranging from 1 to 55 for the AGNR, ZGNR and 2DEG. When $N > 10$, Fig. 3(b) presents a plateau close to $\gamma = 1$ for the three types of ELG, which indicates regular diffusive transport. On the other hand, when $N < 10$ the honeycomb and square lattices behave differently. For AGNR and ZGNR, we have a plateau close to $\gamma = 0.5$, which is consistent with Lévy transport. However, for the 2DEG with $N < 10$, the average transmission can no longer be fitted by Eq. (1). Instead, they follow an exponential, which is compatible with Anderson localization [43].

The results of Fig. 3(b) confirm the presence of a Lévy-to-diffusive transition in graphene nanoribbons imbedded into the EQDC. This transition is an exclusive feature of honeycomb lattices, it does not depend on the edge type, and can be tuned by the Fermi energy. However, in order to access this transition in Fig. 3(b) we had to produce an ensemble with 6000 samples, which makes the effect experimentally inaccessible.

Nonetheless, a viable experimental setup can be realized with only one ELG, by linearly increasing the electrostatic potential V from $0.23t_0$ to $0.27t_0$, forming a fictional time series $T(V)$ with 6000 time steps [44 and 45]. We calculated the average transmission as a function of length L from the time series and extracted the

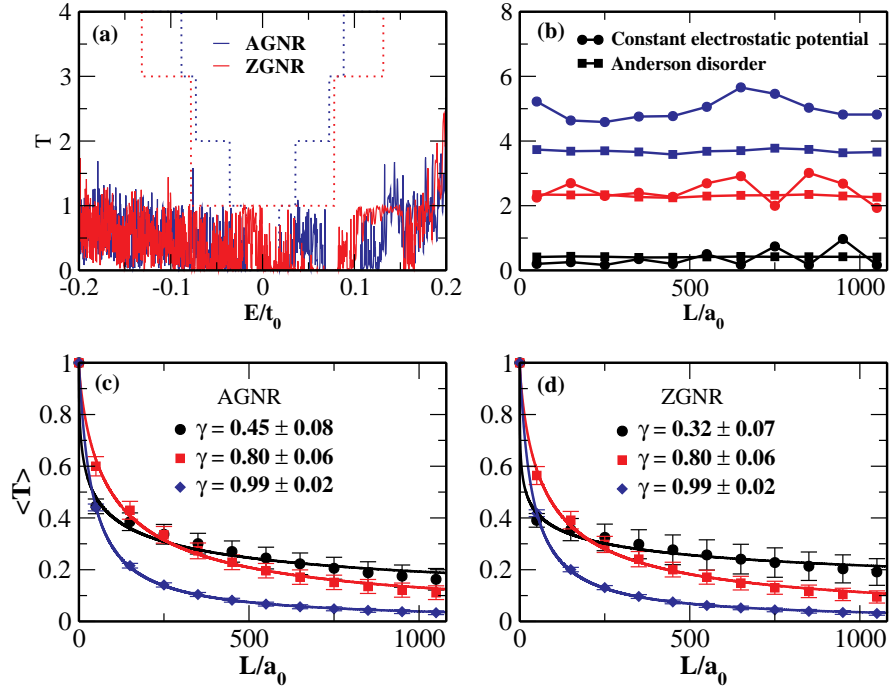


FIG. 2. (a) Transmission through the ELG as a function of Fermi energy (solid lines); dotted lines are for the pristine nanoribbons. (b) Transmission as a function of length L for three different energies (increasing from bottom to top). The circles are for AGNR with constant electrostatic potential $\epsilon_i = V$ in all sites, while squares are for AGNR with Anderson disorder. (c) Average transmission as a function of length L for AGNR, with Fermi energy $E/t_0 = 0.2$ (circles), 0.34 (squares) and 1.2 (diamonds); (d) same for ZGNR, with $E/t_0 = 0.2$ (circles), 0.4 (squares) and 1.2 (diamonds). Solid lines in (c) and (d) are fits obtained from Eq. (1).

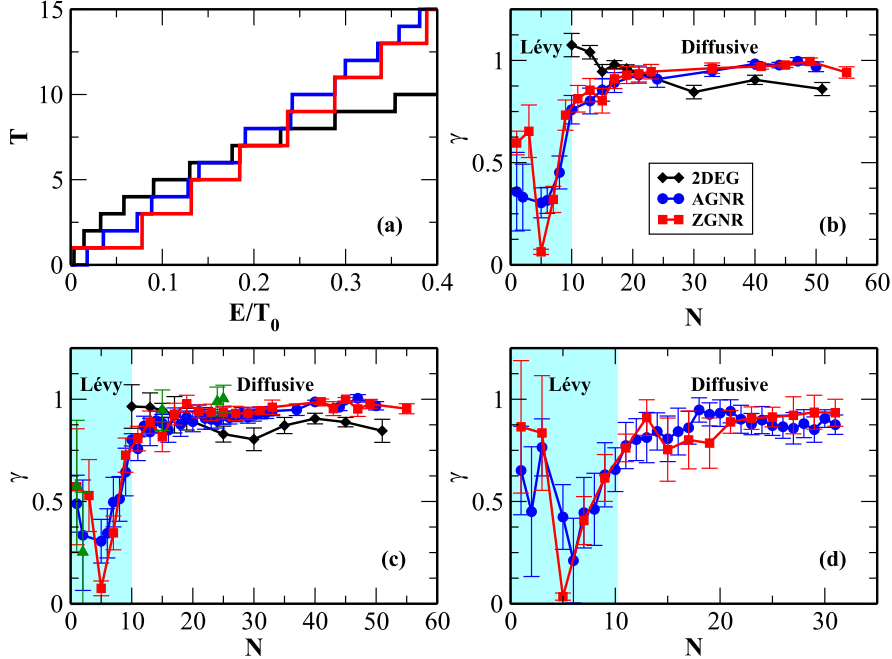


FIG. 3. (a) Transmission versus Fermi energy. The value at the plateaus corresponds to the number of channels N in the AGNR, ZGNR and 2DEG leads. The exponent γ as a function of N for: (b) a set of ELG samples with $W_A = 49.5a_0$, $W_Z = 49.6a_0$ and $W_{2D} = 50a_0$; (c) just one ELG sample with $W_A = 49.5a_0$, $W_Z = 49.6a_0$ and $W_{2D} = 50a_0$. (Triangular symbols are for an AGNR device with second-nearest-neighbor hopping); (d) one ELG sample with $W_A = 59.5a_0$ and $W_Z = 60.0a_0$. Solid lines in (b), (c) and (d) are just to guide the eyes.

exponent γ , shown in Fig. 3(c). The results of Fig. 3(b), obtained from 6000 different samples, and those of Fig. 3(c), obtained from only one sample, are fully compatible, which shows the robustness of the Lévy-to-diffusive transport transition.

In order to further assert the robustness of the transition, we developed a numerical calculation including hopping parameters between second-nearest-neighbors [7]. The triangular symbols in Fig. 3(c) correspond to the data for an AGNR including second-nearest-neighbor hopping with energy $t'_0 = 0.1t_0$ [7]. As expected, we see a Lévy-to-diffusive transport transition, which shows that the inclusion of second-nearest-neighbor hopping does not change our results. Finally, we also increased the width of the nanoribbons to $W_A = 59.5a_0$ and $W_Z = 60.0a_0$, and implemented the one sample procedure described above to obtain Fig. 3(d). Once again, the Lévy-to-diffusive transition is visible in both cases, and is not suppressed by an increase in ribbon width, as we asserted above.

The experiments in Ref. [1] demonstrate a high degree of precision and control over the electrostatic cluster deposition process, capable of avoiding overlap between individual clusters. Nonetheless, we expect our results to remain unchanged for a low cluster overlap density. However, in the case of large cluster overlap, the nanoribbon will approach a situation of constant electrostatic potential in all sites, and we expect its transmission will become similar to the one in Fig. 2(b) (circles).

IV. DISCUSSION

A graphene nanoribbon imbedded in an EQDC shows a Lévy-to-diffusive transport transition as a function of Fermi energy. The transport is superdiffusive in the quantum regime, i.e. $N < 10$, and diffusive in the semiclassical regime, $N > 10$ [44 and 46]. Ref. [47] showed that the transmission fluctuations of graphene as a function of magnetic field are multifractal close to the Dirac point and monofractal far away from it. This multifractality has its origin in the quantum correlations induced by an external parameter such as a magnetic field or electrostatic potential, which decreases as the number of channels N (or the Fermi energy) increases [44]. Nonetheless, graphene presents a linear energy dispersion close to the Dirac point, which preserves chiral symmetry. However, both linear dispersion and chiral symmetry are broken by increasing the Fermi energy [48–50].

Given this scenario, what could possibly be the origin of our Lévy-to-diffusive transport transition? We list two potential causes: 1) loss of multifractality induced by the increase of the Fermi energy; 2) chiral symmetry breaking also induced by an increase in Fermi energy. In what follows, we critically examine both possibilities and conclude that our results are most compatible with the second one.

In order to answer the question above, and understand

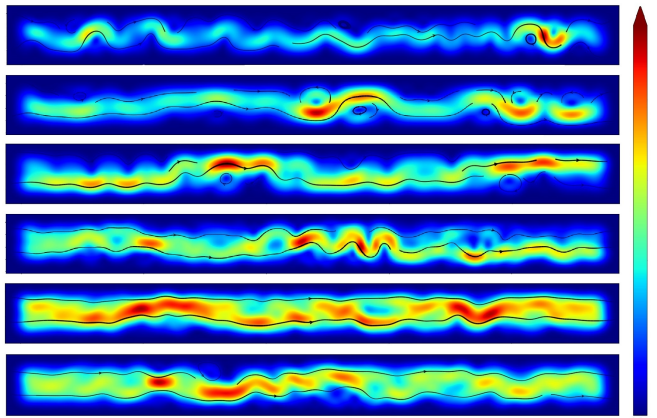


FIG. 4. Current density for an AGNR with $L_A = 1050.7a_0$ and $N = 1, 2, 5, 10, 20$ and 47 (top to bottom). Current density increases as the color changes from blue to red.

the electronic transport in both regimes, we analyzed the current density of AGNR with $L_A = 1050.7a_0$ and $N = 1, 2, 5, 10, 20$ and 47 (top to bottom), as shown in Fig. 4. The current flow deviates from the electrostatic quantum dots in the quantum regime $N < 10$, due to the multifractality of the transmission, accompanied by the slow transmission dynamic [51], i.e., Lévy transport. Besides, the Lévy transport regime gives rise to vortexes surrounding the smaller quantum dots. Those vortexes are an evidence of turbulence-like behavior in an integer quantum Hall transition, as reported in Ref. [45]. Meanwhile, in the semiclassical regime $N > 10$, the current flow fills all of the ELG due to the fast transmission dynamic and destroys the vortexes, compatible with a regular diffusive regime. We have obtained similar results for a ZGNR.

We can understand the slow and fast dynamics, i.e., Lévy-to-diffusive transition, using the fictional time series $T(V)$. Fig. 5(a) shows the histogram of the transmission velocity, defined as $\Delta T/\Delta V$ [52], where $\Delta T = T(V + \Delta V) - T(V)$. The data corresponds to an AGNR with $L_A = 1050.7a_0$ and $N = 1, 10$ and 33 . For $N = 1$ we have a non-Gaussian distribution (black circles) with a narrow peak around zero and heavy tails, while for $N = 10$ and 33 the distribution approaches a Gaussian. According to Ref.[44], this transition from non-Gaussian to Gaussian behavior is due to the loss of multifractality induced by the increase of the Fermi energy. On the other hand, the inset of Fig. 5(a) shows that the 2DEG sample also presents a transition from non-Gaussian to Gaussian distribution, which indicates that the loss of multifractality is not an exclusive feature of the honeycomb lattice. Hence, we can conclude that the loss of multifractality cannot be the cause of our transition, since it is not an exclusive feature of the honeycomb lattice.

Although the loss of multifractality is not the cause of the Lévy-to-diffusive transition, we can still use the histograms to characterize it. The histograms of Fig. 5(a)

can be fitted by q -Gaussian probability density functions

$$P(x) = \frac{\sqrt{\beta}}{C_q} [1 + (q-1)\beta(x-x_0)^2]^{-\frac{1}{q-1}} \quad (6)$$

with

$$C_q = \frac{\sqrt{\pi} \Gamma\left(\frac{3-q}{2(q-1)}\right)}{\sqrt{q-1} \Gamma\left(\frac{1}{q-1}\right)},$$

where $1 < q < 3$, β is a measure of the width of the distribution, and x_0 its mean. We remark that Eq. (6) can be formally derived from a maximization of the Tsallis entropy [53], and note that, when $q \rightarrow 1$, $P(x)$ converges to the Gaussian distribution. Therefore, values of q different from 1 can be seen as a measure of non-Gaussianity.

The solid lines in Fig. 5(a) represent the best fits to Eq. (6), and it is apparent that q decreases as N increases, making it possible to associate the transmission exponent γ with the parameter q . Fig. 5(b) shows the exponent γ as a function of q , where the Lévy-to-diffusive transition is apparent around $q = 3/2$, for both AGNR and ZGNR. When $q < 3/2$ the transmission is diffusive and monofractal, while for $q > 3/2$ it is superdiffusive and multifractal. As reported by Refs. [54–56], the transition from a non-Gaussian to a Gaussian distribution is often associated with a phase transition. Therefore, Fig. 5(b) is strong evidence that the Lévy-to-diffusive transition is a non-equilibrium phase transition.

The main feature of the graphene honeycomb lattice is its linear energy dispersion close to the Dirac point, while the square lattice has a parabolic dispersion. As a consequence of the linear dispersion, charge carriers behave as relativistic massless Dirac fermions and can tunnel through electrostatic potential barriers with null reflection probability, i.e., Klein tunneling effect. However, the linear dispersion is lost far from the Dirac point, due to an increase of Fermi energy, hence, the charge carriers behave as massive fermions.

We can also interpret this behavior in the context of Random Matrix Theory [57]. The electronic transport through the honeycomb lattice in the absence of a magnetic field and spin-orbit interaction is described by the BDI class of Chiral Ensembles, while for the square lattice it is described by the AI class of Wigner-Dyson Ensembles at Cartan's nomenclature [49]. The honeycomb lattice preserves time-reversal, particle-hole, and chiral symmetries at the Dirac point [49]. However, far away from it, the BDI class crosses over to the AI class because of the chiral symmetry breaking [48–50]. This explains the different behavior between honeycomb and square lattices in the quantum regime $N < 10$, and the similar behavior in the semiclassical regime $N > 10$ shown in the Fig. 3(b) and (c).

Thus, we are led to conclude that the superdiffusive transport is an exclusive feature of ELG in the quantum regime, while diffusive transport is a feature in the semiclassical regime. Therefore, the most compelling explanation for the observed Lévy-to-diffusive transition in

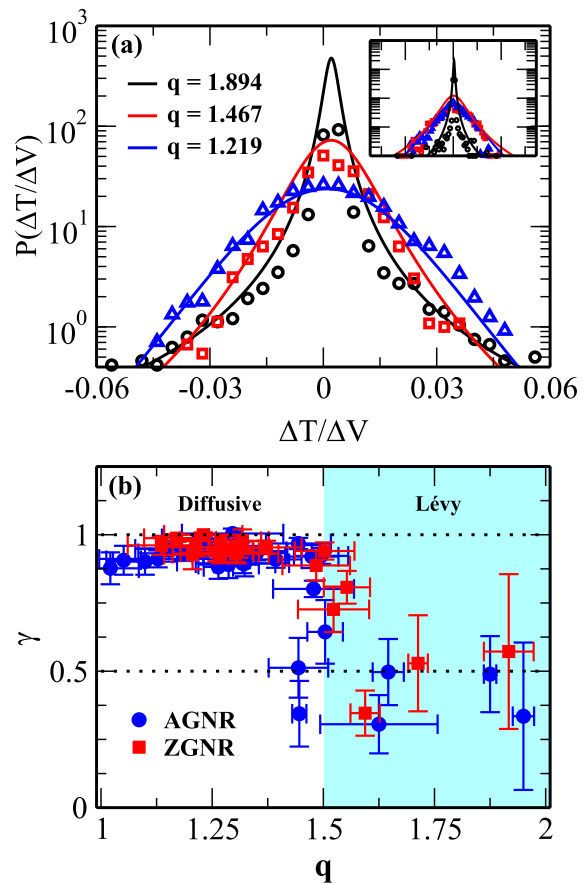


FIG. 5. (a) Histogram of the transmission velocity $\Delta T/\Delta V$ and its respective q -Gaussian fits from Eq. (6) for AGNR superlattices with $W_A = 49.5a_0$ and $L_A = 1050.7a_0$ with $N = 1$ (black), 10 (red) and 33 (blue). The inset shows the histogram of $\Delta T/\Delta V$ for a 2DEG sample. (b) The exponent γ as a function of the parameter q , for AGNR and ZGNR.

our calculations is the chiral symmetry breaking. Furthermore, Refs. [58 and 59] indicate that chiral symmetry breaking has been associated with a phase transition, reinforcing that our transport transition can be a non-equilibrium phase transition associated with chiral symmetry breaking and, hence, the loss of linear energy dispersion.

Finally, it is interesting to compare our findings with those in Ref.[20]. Light has a linear energy dispersion similar to graphene close to the Dirac point. Thus, when light is submitted to an optical material in which its transport is governed by Lévy statistics, it leaves the regular diffusive regime and enters the Lévy one. However, light is not expected to show a Lévy-to-diffusive transition because its dispersion is always linear, unlike that of graphene.

V. CONCLUSIONS

In conclusion, we proposed an electronic Lévy glass, analogous to a recent optical realization. We investigated the transmission of electrons in AGNR and ZGNR in the presence of circular electrostatic clusters, whose diameter follow a power-law distribution. We analyzed the effect of the EQDC on the electronic transport of nanoribbons and its diffusion regime, in comparison to a 2DEG. Our numerical calculations showed that the presence of the clusters induces a transition from Lévy (superdiffusive) to regular diffusive transport as the Fermi energy increases, which was verified by a q-Gaussian analysis, as shown in Fig. 5(b). We conclude that the superdiffusive transport in ELG is an exclusive feature of the low-energy quantum regime, while diffusive transport is a feature of the semiclassical regime. Therefore, the observed Lévy-to-diffusive transport transition is mostly likely caused by chiral symmetry breaking once we move away from the

graphene Dirac point. It would be interesting to investigate how the shape of the EQDC affects the electronic transport behavior and if the superdiffusive regime also appears in the case of non-circular clusters.

ACKNOWLEDGEMENTS

DBF acknowledges a scholarship from Fundação de Amparo a Ciência e Tecnologia de Pernambuco (FACEPE, Grant IBPG-0253-1.04/22). LFCP acknowledges financial support from Conselho Nacional de Desenvolvimento Científico e Tecnológico (CNPq, Grants 436859/2018 and 313462/2020), and FACEPE (Grant APQ-1117-1.05/22). ALRB also acknowledges financial support from CNPq (Grant 309457/2021). We would like to thank C. W. J. Beenakker for bringing Ref. [36] to our attention and for his useful suggestions.

-
- * luiz.cpereira@ufpe.br
 † anderson.barbosa@ufrpe.br
- ¹ J. M. Caridad, S. Connaughton, C. Ott, H. B. Weber, and V. Krstić, *Nature Communications* **7**, 12894 (2016).
 - ² Z. Wu, F. Zhai, F. M. Peeters, H. Q. Xu, and K. Chang, *Phys. Rev. Lett.* **106**, 176802 (2011).
 - ³ H.-Y. Xu, G.-L. Wang, L. Huang, and Y.-C. Lai, *Phys. Rev. Lett.* **120**, 124101 (2018).
 - ⁴ V. V. Cheianov, V. Fal'ko, and B. L. Altshuler, *Science* **315**, 1252 (2007), <https://www.science.org/doi/pdf/10.1126/science.1138020>.
 - ⁵ K. S. Novoselov, A. K. Geim, S. V. Morozov, D. Jiang, Y. Zhang, S. V. Dubonos, I. V. Grigorieva, and A. A. Firsov, *Science* (80-.). **306**, 666 (2004).
 - ⁶ K. S. Novoselov, A. K. Geim, S. V. Morozov, D. Jiang, M. I. Katsnelson, I. V. Grigorieva, S. V. Dubonos, and A. A. Firsov, *Nature* **438**, 197 (2005).
 - ⁷ A. H. Castro Neto, F. Guinea, N. M. R. Peres, K. S. Novoselov, and A. K. Geim, *Rev. Mod. Phys.* **81**, 109 (2009).
 - ⁸ M. I. Katsnelson, K. S. Novoselov, and A. K. Geim, *Nature Physics* **2**, 620 (2006).
 - ⁹ A. L. R. Barbosa, J. R. F. Lima, and L. F. C. Pereira, *Phys. Rev. E* **106**, 054127 (2022).
 - ¹⁰ R. L. Heinisch, F. X. Bronold, and H. Fehske, *Phys. Rev. B* **87**, 155409 (2013).
 - ¹¹ J. H. Bardarson, M. Titov, and P. W. Brouwer, *Phys. Rev. Lett.* **102**, 226803 (2009).
 - ¹² C. Gutiérrez, L. Brown, C.-J. Kim, J. Park, and A. N. Pasupathy, *Nature Physics* **12**, 1069 (2016).
 - ¹³ H. Fehske, G. Hager, and A. Pieper, *physica status solidi (b)* **252**, 1868 (2015), <https://onlinelibrary.wiley.com/doi/pdf/10.1002/pssb.201552119>.
 - ¹⁴ M. Sadrara and M. Miri, *Physical Review B* **99**, 155432 (2019).
 - ¹⁵ J. D. Walls and D. Hadad, *Scientific Reports* **5**, 8435 (2016).
 - ¹⁶ J. D. Walls and D. Hadad, *Scientific Reports* **6**, 26698 (2016).
 - ¹⁷ V. Jakubský, i. m. c. Kuru, and J. Negro, *Phys. Rev. B* **105**, 165404 (2022).
 - ¹⁸ S.-Y. Li and L. He, *Frontiers of Physics* **17**, 33201 (2021).
 - ¹⁹ M. Sadrara and M. Miri, *Journal of Physics: Condensed Matter* **34**, 115703 (2022).
 - ²⁰ P. Barthelemy, J. Bertolotti, and D. S. Wiersma, *Nature* **453**, 495 (2008).
 - ²¹ V. Zaburdaev, S. Denisov, and J. Klafter, *Reviews of Modern Physics* **87**, 483 (2015).
 - ²² M. E. Wosniack, M. C. Santos, E. P. Raposo, G. M. Viswanathan, and M. G. E. da Luz, *PLOS Computational Biology* **13**, 1 (2017).
 - ²³ N. Levernier, J. Textor, O. Bénichou, and R. Voituriez, *Phys. Rev. Lett.* **124**, 080601 (2020).
 - ²⁴ T. H. Solomon, E. R. Weeks, and H. L. Swinney, *Phys. Rev. Lett.* **71**, 3975 (1993).
 - ²⁵ N. Mercadier, W. Guerin, M. Chevrollier, and R. Kaiser, *Nature Physics* **5**, 602 (2009).
 - ²⁶ A. A. Fernández-Marín, J. A. Méndez-Bermúdez, J. Carbonell, F. Cervera, J. Sánchez-Dehesa, and V. A. Gopar, *Phys. Rev. Lett.* **113**, 233901 (2014).
 - ²⁷ A. A. Fernández-Marín, J. A. Méndez-Bermúdez, and V. A. Gopar, *Phys. Rev. A* **85**, 035803 (2012).
 - ²⁸ L. A. Razo-López, A. Z. Genack, and V. A. Gopar, *Phys. Rev. Research* **3**, 023035 (2021).
 - ²⁹ J. Li, H. Wu, Z. Wang, S. Lin, C. Lu, E. P. Raposo, A. S. L. Gomes, and Y. Rao, *Opt. Lett.* **44**, 2799 (2019).
 - ³⁰ M. Leadbeater, V. I. Falko, and C. J. Lambert, *Phys. Rev. Lett.* **81**, 1274 (1998).
 - ³¹ S. Gattenlöhner, I. V. Gornyi, P. M. Ostrovsky, B. Trauzettel, A. D. Mirlin, and M. Titov, *Phys. Rev. Lett.* **117**, 046603 (2016).
 - ³² E. I. Kiselev and J. Schmalian, *Phys. Rev. Lett.* **123**, 195302 (2019).
 - ³³ J. R. F. Lima, L. F. C. Pereira, and A. L. R. Barbosa, *Phys. Rev. E* **99**, 032118 (2019).

- ³⁴ A. V. Chechkin, F. Seno, R. Metzler, and I. M. Sokolov, *Phys. Rev. X* **7**, 021002 (2017).
- ³⁵ K. Vynck, R. Pierrat, R. Carminati, L. S. Froufe-Pérez, F. Scheffold, R. Sapienza, S. Vignolini, and J. J. Sáenz, “Light in correlated disordered media,” (2021).
- ³⁶ C. W. Groth, A. R. Akhmerov, and C. W. J. Beenakker, *Phys. Rev. E* **85**, 021138 (2012).
- ³⁷ P. Barthelemy, *Anomalous Transport of Light*, Ph.D. thesis, Citeseer (2009).
- ³⁸ S. Datta, *Quantum transport: atom to transistor* (Cambridge university press, 2005).
- ³⁹ C. W. Groth, M. Wimmer, A. R. Akhmerov, and X. Waintal, *New Journal of Physics* **16**, 063065 (2014).
- ⁴⁰ I. Amanatidis, I. Klefogiannis, F. Falceto, and V. A. Gopar, *Phys. Rev. E* **96**, 062141 (2017).
- ⁴¹ K. Nomura, M. Koshino, and S. Ryu, *Physical review letters* **99**, 146806 (2007).
- ⁴² C. H. Lewenkopf, E. R. Mucciolo, and A. C. Neto, *Physical Review B* **77**, 081410 (2008).
- ⁴³ P. Sheng and B. van Tiggelen, “Introduction to wave scattering, localization and mesoscopic phenomena.” (2007).
- ⁴⁴ N. Pessoa, A. Barbosa, G. Vasconcelos, and A. Macedo, *Physical Review E* **104**, 054129 (2021).
- ⁴⁵ A. L. R. Barbosa, T. H. V. de Lima, I. R. R. González, N. L. Pessoa, A. M. S. Macêdo, and G. L. Vasconcelos, *Phys. Rev. Lett.* **128**, 236803 (2022).
- ⁴⁶ L. H. Oliveira, A. L. R. Barbosa, and M. Novaes, *Journal of Physics A: Mathematical and Theoretical* **55**, 375202 (2022).
- ⁴⁷ K. R. Amin, S. S. Ray, N. Pal, R. Pandit, and A. Bid, *Communications Physics* **1** (2018), 10.1038/s42005-017-0001-4.
- ⁴⁸ S. Gnutzmann and B. Seif, *Phys. Rev. E* **69**, 056219 (2004).
- ⁴⁹ P. Jacquod, R. S. Whitney, J. Meair, and M. Büttiker, *Phys. Rev. B* **86**, 155118 (2012).
- ⁵⁰ M. S. M. Barros, A. J. N. Júnior, A. F. Macedo-Junior, J. G. G. S. Ramos, and A. L. R. Barbosa, *Phys. Rev. B* **88**, 245133 (2013).
- ⁵¹ A. Duthie, S. Roy, and D. E. Logan, *Phys. Rev. B* **106**, L020201 (2022).
- ⁵² P. W. Brouwer, S. A. van Langen, K. M. Frahm, M. Büttiker, and C. W. J. Beenakker, *Phys. Rev. Lett.* **79**, 913 (1997).
- ⁵³ H. Suyari, *Physica A: Statistical Mechanics and its Applications* **368**, 63 (2006).
- ⁵⁴ V. Latora, A. Rapisarda, and C. Tsallis, *Phys. Rev. E* **64**, 056134 (2001).
- ⁵⁵ A. Pluchino, A. Rapisarda, and C. Tsallis, *Europhysics Letters (EPL)* **80**, 26002 (2007).
- ⁵⁶ I. R. R. González, B. C. Lima, P. I. R. Pincheira, A. A. Brum, A. M. S. Macêdo, G. L. Vasconcelos, L. de S. Menezes, E. P. Raposo, A. S. L. Gomes, and R. Kashyap, *Nature Communications* **8**, 15731 (2017).
- ⁵⁷ C. W. J. Beenakker, *Rev. Mod. Phys.* **69**, 731 (1997).
- ⁵⁸ M. V. Ulybyshev, P. V. Buividovich, M. I. Katsnelson, and M. I. Polikarpov, *Phys. Rev. Lett.* **111**, 056801 (2013).
- ⁵⁹ C. Bao, H. Zhang, T. Zhang, X. Wu, L. Luo, S. Zhou, Q. Li, Y. Hou, W. Yao, L. Liu, P. Yu, J. Li, W. Duan, H. Yao, Y. Wang, and S. Zhou, *Phys. Rev. Lett.* **126**, 206804 (2021).